ISSN: 2690- 912X

Research Article

Journal of Genetic Engineering and Biotechnology Research

Investigation of a Very Sensitive Refractive Index Sensor Based on Waveguide TM Mode Resonance and Design of a Plasmatic Sensor

Hamid Abbasi

University of Mazandaran, Iran

*Corresponding Author
Hamid Abbasi, University of Mazandaran, Iran.

Submitted: 28 Sep 2022; **Accepted:** 18 Oct 2022; **Published:** 07 Apr 2023

Citation: Abbasi, H. (2023). Investigation of a Very Sensitive Refractive Index Sensor Based On Waveguide Tm Mode Resonance and Design of a Plasmatic Sensor. *J Gene Engg Bio Res, 5*(1), 58-65.

Abstrac

This study proposes a highly sensitive refractive index sensor based on the TM wavelength resonance excited in a structure of a plasmonic sensor. The results show that the resonance wavelength will shift significantly with increasing and changing the refractive index, which shows that this method can be used to understand the resonance wavelength and refractive index. Based on this approach, the sensing characteristics, including the sensitivity and the figure of merit (FOM) and the Q quality factor, have been investigated, where the sensor sensitivity has reached 1165 nm / RIU. Compared to plasmon surface resonance sensors, which are based on a similar structure, the proposed sensor can achieve a more flexible range of wavelengths and a wider range of refractive index. Therefore, this method has tremendous potential for use in various fields of measurement, such as biochemical analysis and medicine, and can find useful applications in measurement systems and integrated circuits. Also, all the diagrams obtained in this research have been drawn using MATLAB program.

Keywords: Plasmonics, Surface Plasmon Polarities, Metal-Insulator Metal, Refractive Index Sensor

Introduction

Surface Plasmon resonance (SPR) can generate a strong electromagnetic field enhancement on the surface of a metal structure, and is very sensitive to the surrounding environment [1, 2]. Therefore, SPR can be applied to numerous fields such as absorption enhancement magnetic field enhancement photocatalysis THz oscillation Fano resonance surface enhanced Raman scattering (SERS) sub-wavelength lithography and refractive index (RI) sensors [3, 4]. For refractive index sensors based on SPR, the resonance is excited mainly in two modes, the angular mode (at fixed wavelength) and the spectral mode (at fixed angle) [5-10]. If the light beam is in a direction where the incidence angle is fixed and the spectrum of the reflectance is probed, is called the spectral interrogation configuration and if the light beam is in a direction in which the wavelength of the incident light can be constant and the angle of incidence (slope of the light line) can be changed, it is called angular navigation configuration. Due to the low efficiency of continuous change of impact angle in a real system, the wavelength scanning method is preferred as a tool for faster measurement of the reflectance spectrum. Therefore, in this paper, we examined the wavelength scanning method, which simultaneously irradiated the analyse with different wavelengths, which showed obvious improvements over the angular-based refractive index measurement method [11-14]. Using fixed-wavelength scanning, the reflection spectrum can be detected using a spectrometer, and the close relationship between Refractive index and the wavelength resonance position can be used to determine refractive index [15-18]. In the following, we examine parameters such as high transmission efficiency, high resolution, high quality coefficient, optical stability, sensitivity (S) and figure of merit (FOM) so that the designed sensor displays an excellent performance with high optical resolution. Obtaining and improving these parameters increases the speed of information processing in optically integrated circuits.

Structural Model and Theory Analysis

The two-dimensional schematic view of the proposed plasmonic refractive index sensor consisting of two waveguides and five cavities with different dimensions and characteristics is shown in Figure 1. Two plasmonic waveguides have a height of $w_1 = 50$ nm. A cavity with a height of $w_2 = 62$ nm and a length of $L_1 = 264$ nm is located in the middle of two waveguides. The two cavities at the top have a height of $w_3 = 220$ nm and $w_4 = 100$ nm, and a length of $L_2 = 100$ nm and $L_3 = 100$ nm, respectively, and the two cavities at the bottom have a height of $w_5 = 100$ nm and $w_6 = 220$ nm, respectively. Length is $L_4 = 100$ nm and $L_5 = 100$ nm. Two monitors, Pin and Pout, are used to measure the input and output waves. The transfer rate is calculated by the following equation:

$$T = P_{out} / P_{in} \quad (1)$$

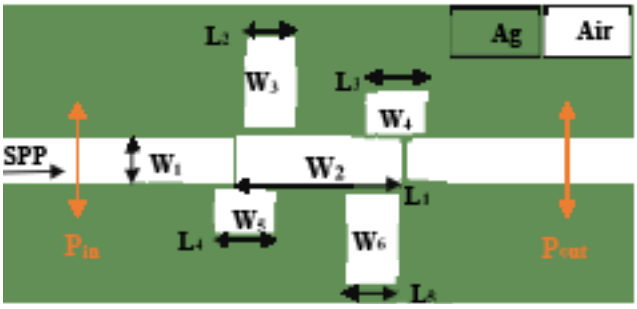

Figure 1: Two-dimensional Image of a Plasmonic Sensor

Now, in order to measure the dimensions and coordinates of the cavities and to show a better sensor, we examine the transmission spectra with different numbers of cavities. According to Figure 2, the transmission spectrum has a higher altitude for the case where only the middle cavity is active, but for the case where all five cavities are active, it has the highest wavelength transfer.

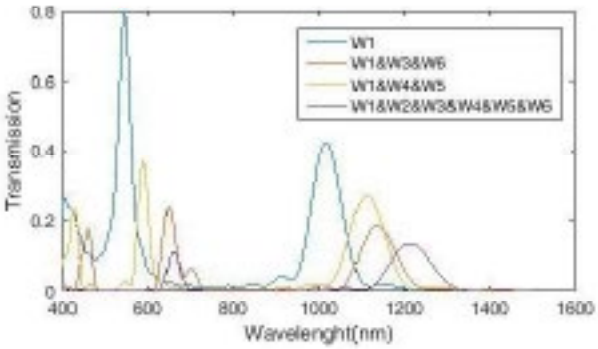

Figure 2: MIM waveguide transmission spectra with five cavities in different coordinates

Sensor Simulation and Design Methods Using Refractive Index Measurement

The proposed plasmonic resonance behaviour is investigated numerically and theoretically. For the numerical approach, we use the time domain finite difference simulation method with perfectly matched layer boundary conditions (PML) because this method effectively reduces the numerical reflection [19-21]. The uniform mesh size for the x and y directions is considered to be 8 and 8 nm, respectively, and the transmission line model is used for structural theory analysis [22-25]. Two-dimensional simulation is performed, which is infinite in one dimension. The reason for this is to reduce the simulation time and achieve the desired result. The simulation is calculated in the wavelength range of 400 to 1600 nm. Because the drude model can be easily integrated in time-difference finite difference simulations, we use the drude model to show the optical properties of metals in simulation:

$$\varepsilon(\omega) = \varepsilon_{\infty} - \frac{{\omega_p}^2}{\omega^2 + i\gamma\omega} \qquad (2)$$

Here ∞ =1 gives the medium constant for the infinite frequency, ω_p = 1.37 × 1016 refers to bulk frequency for plasma, γ = 3.21 × 1013 means damping frequency for electron oscillation, and ω shows incident light angular frequency. The TM wave starts moving from the left and propagates in the waveguide, and the closer it gets to the output port, the lower its intensity. This beam of light that hits the metal surface from the air, never stimulates Plasmon on the joint surface of the metal, unless the light beam momentum increases to match the surface plasmon momentum and obtain an intersection between two lines. This intersection reflects the resonance phenomenon and specifies the operating point at which the frequency and vector of the excited light wave and the plasmon are determined. As shown in Figure 3, the middle cavity absorbs the largest amount of TM wave. It also has the most field exchange with waveguides. When the field distribution in the structure is similar, the energy loss is reduced. To achieve the maximum field distribution in the simulated structure, all dimensions must be optimized.

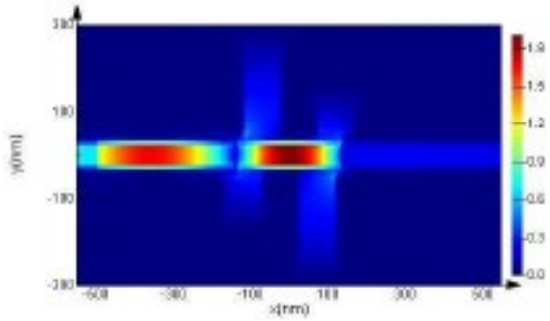

Figure 3: Electric field distribution at resonant frequency **4. Simulation and design of a sensor using two waveguides and a cavity** now we do the simulation only for the middle cavity (Fig.4).

Two-dimensional Image of a Plasmonic Sensor with Two Waveguides and a Cavity

First, to find the optimal structure, we change its length and width. The diagrams related to the change in length and width of the cavity are shown in Fig.5. We choose a height of 62 nm and a length of 264 nm for the middle cavity because the cavity in these points has a higher height and more wavelength change.

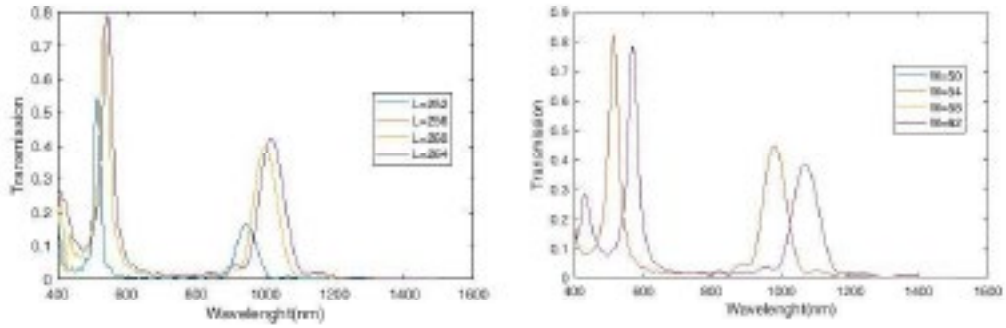

Figure 5: Diagrams related to the change in length and width of the middle cavity

We now increase the refractive index of the middle cavity by a step of 0.01 from 1.14 to 1.2, which leads to a change in the resonance spectra and wavelength. We see the transmission spectrum resulting from changing the sensor refractive index in Fig.6.

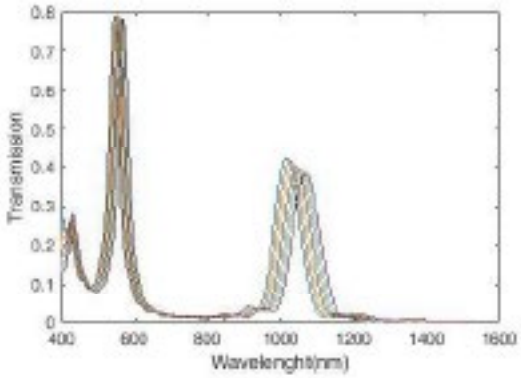

Figure 6: Plasmonic refractive index sensor transmission spectra

To measure the performance of a plasmonic sensor, we need to consider several criteria.The first criterion is the sensitivity S, which is described as the change in resonance wavelength when the dielectric changes unit:

$S = \Delta\lambda / \Delta n$ (nm / RIU) (3) In this equation, $\Delta\lambda$ is the change in resonance wavelength, Δn is the change in refractive index. We see the sensitivity coefficient diagram of the plasmonic sensor in Fig.7. The maximum sensitivity for the refractive index is n = 1.18 (in mode2), which is equal to 1009 nm / RIU.

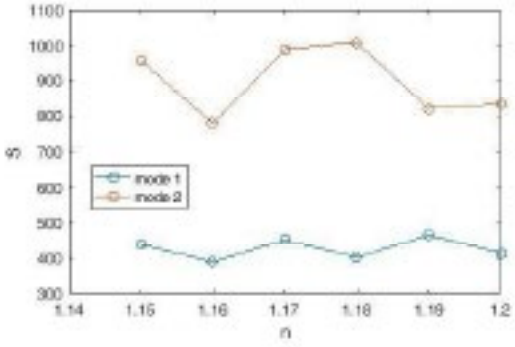

Figure 7: Plasmonic Sensor Sensitivity Coefficient Diagram

The next criterion is the competency digit (FOM) whose equation is as follows:

FOM = S / FWHM (4(The FOM eligibility figure for the plasmonic sensor is plotted in Fig.8. According to the figure, the maximum fitness figure of merit (FOM) for the refractive index is n = 1.16 (in mode2), which is equal to 13.368 nm / RIU.

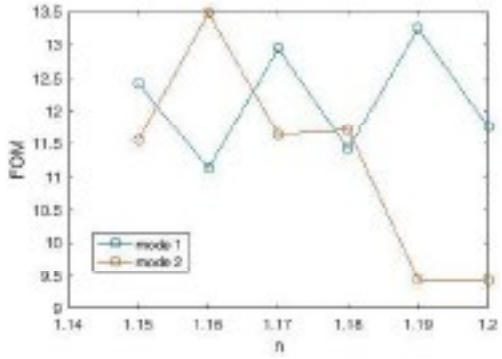

Figure 8: Plasmonic Sensor Figure of Merit (FOM)

The last criterion is the quality factor Q, which is obtained according to Equation 5:

Q = λres / FWHM (5(We see the diagram of the quality coefficient of the plasmonic sensor in Fig.9. According to the figure, the highest quality factor Q is for the refractive index n = 1.2 (in mode1), which is equal to 16.187 nm / RIU.

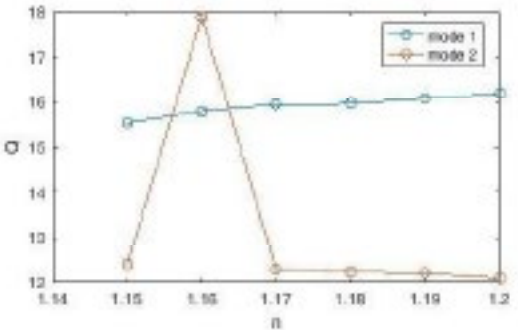

Figure 9: Plasmonic Sensor Quality Coefficient Diagram

Simulation and Sensor Design Using Two Waveguides and Three Cavities

Now we add two cavities to the sensor structure and measure its performance (Fig.10).

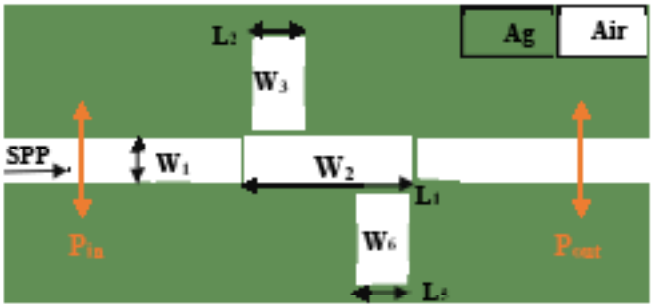

Figure 10: Two-Dimensional Image of a Plasmonic Sensor with Two Waveguides and Three Cavities

We change the refractive index of the middle cavity with a step of 0.01 from 1.14 to 1.2 and the refractive index of the waveguides and the other two cavities remain constant. Fig.11 shows the resulting transmission spectrum, which has three modes, in the wavelength range of 400 to 1600 nm.

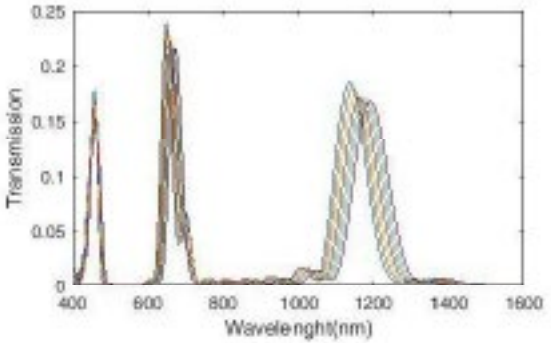

Figure 11: Plasmonic Refractive Index Sensor Transmission Spectra for Three Cavities

We now calculate the sensitivity of the sensor, which according to Fig.12 has the highest sensitivity for the refractive index n = 1.2 (in mode 3), which is equal to 1018 nm / RIU.

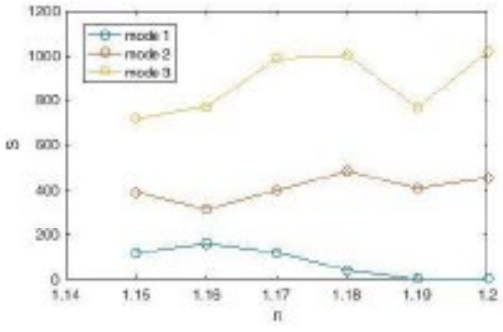

Figure 12: Plasmonic Sensor Sensitivity Coefficient Diagram with Three Cavities

Next, we calculate the FIT and the quality factor Q and draw the corresponding diagrams (Fig.13). According to the figure, the highest figure of merit (FOM) for the refractive index is n = 1.18 (in mode2) which is equal to 12.483 nm / RIU and the highest quality factor Q for the refractive index is n = 1.15 (in mode2) which is equal to With 19.089 nm / RIU.

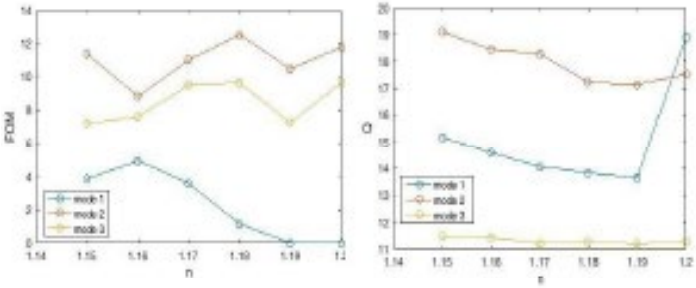

Figure 13: figure of merit (FOM) and Q coefficient diagram of plasmonic sensor with three cavities

Next, we change the structure of the sensor and change the coordinates and dimensions of the two upper and lower cavities (Fig.14), to measure the quality of the sensor and create a suitable structure for the sensor.

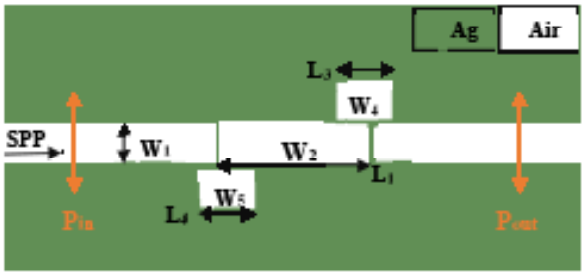

Figure 14: Two-dimensional Image of a Plasmonic Sensor with Two Waveguides and Three Cavities

As in the previous structure, we change the refractive index of the middle cavity by a step of 0.01 from 1.14 to 1.2 and the refractive index of the rest of the sensor structure remains constant. The transmission spectrum from the simulation can be seen in Fig.15. This spectrum, which is displayed in the wavelength range of 400 to 1600 nm, has three modes. Mode 3 on the right side of the chart has more flexibility than changing the wavelength [26, 27].

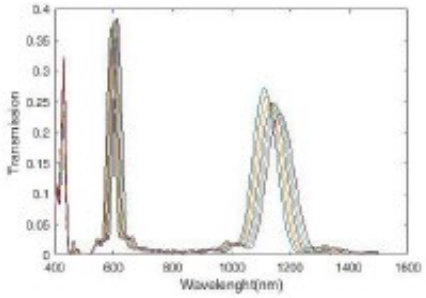

Figure 15: Plasmonic Refractive Index Sensor Transmission Spectra for Three Cavities

We now move on to measuring the sensor designed in Fig.14 and computing the sensitivity coefficient, quality factor Q, and the figure of merit (FOM). First the coefficient diagram we obtain the sensitivity, which according to Fig.16, the highest sensitivity is obtained at a refractive index of n = 1.16 (in mode3), which is equal to 1165 nm / RIU. Compared to the highest sensitivity obtained from the sensor in Fig.10, this sensor has better performance and has reached a higher sensitivity. Therefore, changing the dimensions and coordinates of the cavities has improved the sensor.

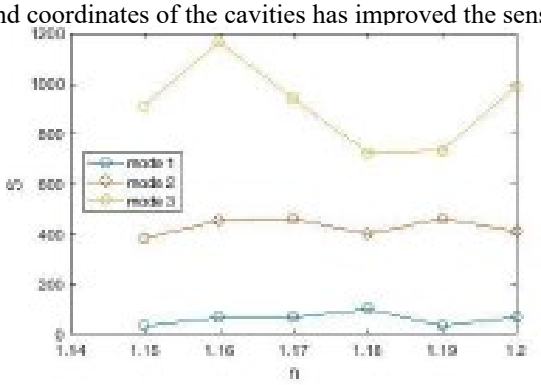

Figure 16: Plasmonic Sensor Sensitivity Coefficient Diagram with Three Cavities

By calculating and plotting the Diagrams of the figure of merit (FOM) and the quality factor Q, the performance measurement of this structure is completed (Fig. 17(. According to the figure, the highest the figure of merit (FOM) for the refractive index is n = 1.17 (in mode 2) which is equal to 15.128 nm / RIU and the highest quality factor Q is for the refractive index n = 1.2 (in mode 1) which is equal to 24.183 nm / RIU [28-30].

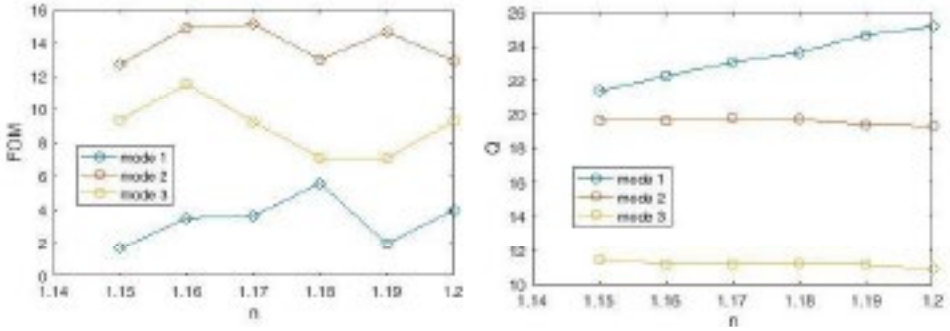

Figure 17: The figure of merit (FOM) diagram and the Q coefficient diagram of plasmonic sensor with three cavities

Simulation and Design of a Sensor Using Two Waveguides and Five Cavities

We now design a combination of the two structures designed in Figures 9 and 13 to obtain a better and more efficient sensor (Fig. 18(.

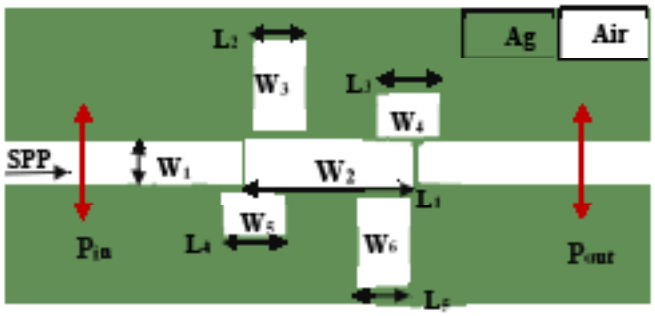

Figure 18: Two-dimensional image of a plasmonic sensor with two waveguides and five cavities

We obtain the transmission spectrum by changing the refractive index of the middle cavity with a step of 0.01 from 1.14 to 1.2 (Fig.19). Here the refractive index of the other four cavities remains constant. This stabilizes the sensor performance and improves its quality. The resulting transmission spectrum has two peaks, with the right peak having more flexibility in changing the wavelength.

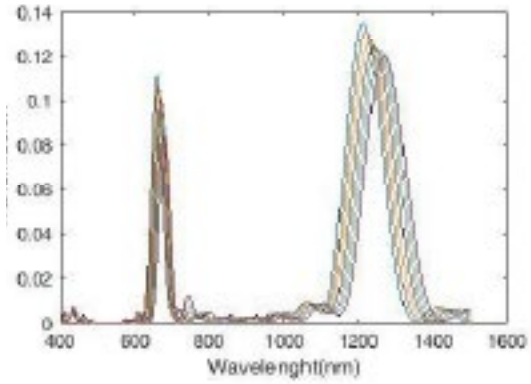

Figure 19: Plasmonic refractive index sensor transmission spectra for five cavities

To analyse the structure of this sensor, we first calculate the sensitivity coefficient in the wavelength range of 400-1600 nm and then draw a graph. The sensitivity coefficient diagram, as the first criterion for measuring the performance of this sensor, shows us that the maximum sensitivity coefficient obtained using the transmission spectra of this sensor is equal to 1124 nm / RIU (Fig.20).

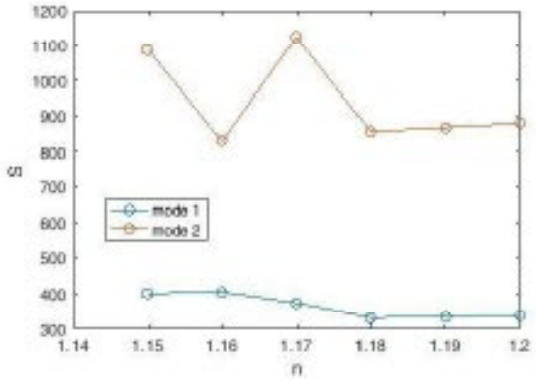

Figure 20: Plasmonic sensor sensitivity coefficient diagram with fine cavities

The next criterion for measuring the performance of the FOM sensor is obtained using Equation 4. Drawing the corresponding diagram (Fig.21), we find that the highest value of Qom is the merit (FOM), with a refractive index of n = 1.15 (in case 1), which is equal to 12.395 nm / RIU.

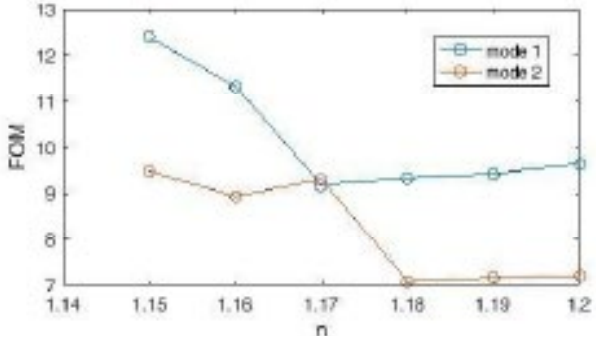

Figure 21: the figure of merit (FOM) diageram for Plasmonic Sensor with Two WaveGuides and Five cavities

The final criterion for measuring the structure of this sensor is the quality factor Q. Using Equation 5, we draw the corresponding diagram (Fig.22). The highest quality factor Q for the refractive index is n = 1.15 (in case 1) which is equal to 20.505 nm / RIU.

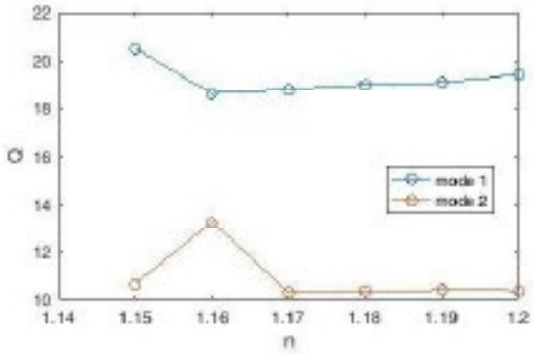

Figure 22: Q quality factor diagram for plasmon sensor with five cavities

Our research on this sensor is over. With the structure that was designed and by changing the coordinates and dimensions of the cavities, we were able to study and analyze our desired sensor in different states and conditions and achieve a stable and balanced structure for making plasmonic sensors.

Conclusion

In this paper, a refractive index sensor based on TM wavelength resonance is investigated. An amplifier system connected to a plasmonic waveguide, consisting of two metal-insulated metal waveguides (MIM) with five cavities, has been designed and numerically evaluated using the Finite Deference Time Domain method. The results show that the resonance wavelength will shift significantly with increasing and changing the refractive index, which suggests that this method can be used to understand the resonance wavelength and refractive index [31-34]. Next, the sensitivity coefficient and FOM competency figure and Q quality coefficient are examined, in which the sensor sensitivity has reached 1124 nm / RIU and 1165 nm / RIU. This means that the sensor, due to its high resolution, can easily analyze the change in refractive index of 0.01 for materials with a refractive index of between 1.14 and 1.2. Also, all the diagrams obtained in this research have been drawn using MATLAB program. Hopefully, the proposed structure will provide guidelines for the design of nano-sensors.

Data Availability

Data sharing is not applicable to this article as no datasets were generated or analyzed during the current study.

Code Availability

Numerical analysis of this paper is based on FDTD method.

Funding information

This study has not any financial support.

Authors' Contributions

All authors have same contribution in the analytical and numerical calculations, read, and approved the final manuscript.

Reference

1. Cen, C., Liu, L., Zhang, Y., Chen, X., Zhou, Z., Yi, Z., & Xiao, S. (2019). Tunable absorption enhancement in periodic elliptical hollow graphene arrays. Optical Materials Express, 9(2), 706-716.
2. Lin, H., Ye, X., Chen, X., Zhou, Z., Yi, Z., Niu, G., & Xiao, S. (2019). Plasmonic absorption enhancement in graphene circular and elliptical disk arrays. Materials Research Express, 6(4), 045807.
3. Chen, J., Zhang, T., Tang, C., Mao, P., Liu, Y., Yu, Y., & Liu, Z. (2016). Optical magnetic field enhancement via coupling magnetic plasmons to optical cavity modes. IEEE Photonics Technology Letters, 28(14), 1529-1532.
4. Chen, J., Tang, C., Mao, P., Peng, C., Gao, D., Yu, Y., & Zhang, L. (2016). Surface-plasmon-polaritons-assisted enhanced magnetic response at optical frequencies in metamaterials. IEEE Photonics Journal, 8(1), 1-7.
5. Zhao, X., Yang, H., Li, S., Cui, Z., & Zhang, C. (2018). Synthesis and theoretical study of large-sized Bi4Ti3O12 square nanosheets with high photocatalytic activity. Materials Research Bulletin, 107, 180-188.
6. Di, L., Yang, H., Xian, T., & Chen, X. (2018). Construction of Z-scheme g-C3N4/CNT/Bi2Fe4O9 composites with improved simulated-sunlight photocatalytic activity for the dye degradation. Micromachines, 9(12), 613.
7. Yan, Y., Yang, H., Zhao, X., Li, R., & Wang, X. (2018). Enhanced photocatalytic activity of surface disorder-engineered CaTiO3. Materials research bulletin, 105, 286-290.
8. Zheng, C., Yang, H., Cui, Z., Zhang, H., & Wang, X. (2017). A novel Bi4Ti3O12/Ag3PO4 heterojunction photocatalyst with enhanced photocatalytic performance. Nanoscale research letters, 12(1), 1-12.
9. Di, L., Yang, H., Xian, T., & Chen, X. (2018). Facile synthesis and enhanced visible-light photocatalytic activity of novel p-Ag3PO4/n-BiFeO3 heterojunction composites for dye degradation. Nanoscale research letters, 13(1), 1-13.
10. Hou, W., & Cronin, S. B. (2013). A review of surface plasmon resonance-enhanced photocatalysis. Advanced Functional Materials, 23(13), 1612-1619.
11. Safari, S., & Jazi, B. (2017). The role of terahertz surface plasmons in the scattering pattern of electromagnetic waves in an unstable elliptical plasma antenna. Physics of Plasmas, 24(7), 072112.
12. Hongmei, D. U., Zhang, L., & Dongao, L. I. (2018). THz plasma wave instability in field effect transistor with electron diffusion current density. Plasma Science and Technology, 20(11), 115001.
13. Dongao, L. I., Zhang, L., & Hongmei, D. U. (2019). The instability of terahertz plasma waves in cylindrical FET. Plasma Science and Technology, 21(4), 045002.
14. Wang, J., Song, C., Hang, J., Hu, Z. D., & Zhang, F. (2017). Tunable Fano resonance based on grating-coupled and graphene-based Otto configuration. Optics Express, 25(20), 23880-23892.
15. Zhang, X., Qi, Y., Zhou, P., Gong, H., Hu, B., & Yan, C. (2018). Refractive index sensor based on fano resonances in plasmonic waveguide with dual side-coupled ring resonators. Photonic Sensors, 8(4), 367-374.
16. Piao, X., Yu, S., Koo, S., Lee, K., & Park, N. (2011). Fano-type spectral asymmetry and its control for plasmonic metal-insulator-metal stub structures. Optics express, 19(11), 10907-10912.
17. Piao, X., Yu, S., & Park, N. (2012). Control of Fano asymmetry in plasmon induced transparency and its application to plasmonic waveguide modulator. Optics express, 20(17), 18994-18999.
18. Liu, G. Q., Yu, M. D., Liu, Z. Q., Liu, X. S., Huang, S., Pan, P. P., ... & Gu, G. (2015). One-process fabrication of metal hierarchical nanostructures with rich Nano gaps for highly-sensitive surface-enhanced Raman scattering. Nanotechnology, 26(18), 185702.
19. Xiang-Xian, W., Xue-Lin, B., Zhi-Yuan, P., Hua, Y., Yun-Ping, Q., & Xiao-Lei, W. (2019). Surface-enhanced Raman scattering effect of composite structure with gold nano-cubes and gold film separated by polymethylmethacrylate film.
20. Yu, M., Huang, Z., Liu, Z., Chen, J., Liu, Y., Tang, L., & Liu, G. (2018). Annealed gold nanoshells with highly-dense hotspots for large-area efficient Raman scattering substrates. Sensors and Actuators B: Chemical, 262, 845-851.
21. Wang, X., Bai, X., Pang, Z., Yang, H., & Qi, Y. (2019). Investigation of surface plasmons in Kretschmann structure loaded with a silver nano-cube. Results in Physics, 12, 1866-1870.
22. Wang, X.X., Pang, Z.Y., Tong, H., Wu, X.X., Bai, X.L., Yang, H., Wen, X.L., Qi, Y.P. (2019). Theoretical investigation of subwavelength structures fabrication based on multiexposure surface Plasmon interference lithography. Results Phys. 12, 732–737.
23. Wang, X., Pang, Z., Tong, H., Wu, X., Bai, X., Yang, H., & Qi, Y. (2019). Theoretical investigation of subwavelength structure fabrication based on multi-exposure surface Plasmon interference lithography. Results in Physics, 12, 732-737.
24. Liang, C., Niu, G., Chen, X., Zhou, Z., Yi, Z., Ye, X., & Xiao, S. (2019). Tunable triple-band graphene refractive index sensor with good angle-polarization tolerance. Optics Communications, 436, 57-62.
25. Liu, C., Su, W., Liu, Q., Lu, X., Wang, F., Sun, T., & Chu, P. K. (2018). Symmetrical dual D-shape photonic crystal fibers for surface plasmon resonance sensing. Optics express, 26(7), 9039-9049.
26. Liu, Z., Yu, M., Huang, S., Liu, X., Wang, Y., Liu, M., & Liu, G. (2015). Enhancing refractive index sensing capability with hybrid plasmonic–photonic absorbers. Journal of Materials Chemistry C, 3(17), 4222-4226.
27. Yun-Ping, Q., Xue-Wei, Z., Pei-Yang, Z., Bing-Bing, H., &

Xiang-Xian, W. (2018). Refractive index sensor and filter of metal-insulator-metal waveguide based on ring resonator embedded by cross structure.
28. Cen, C., Lin, H., Huang, J., Liang, C., Chen, X., Tang, Y., & Xiao, S. (2018). A tunable plasmonic refractive index sensor with nanoring-strip graphene arrays. Sensors, 18(12), 4489.
29. Liu, C., Yang, L., Lu, X., Liu, Q., Wang, F., Lv, J., & Chu, P. K. (2017). Mid-infrared surface plasmon resonance sensor based on photonic crystal fibers. Optics express, 25(13), 14227-14237.
30. Abutoama, M., & Abdulhalim, I. (2015). Self-referenced biosensor based on thin dielectric grating combined with thin metal film. Optics express, 23(22), 28667-28682.
31. Abutoama, M., & Abdulhalim, I. (2017). Angular and intensity modes self-referenced refractive index sensor based on thin dielectric grating combined with thin metal film. IEEE Journal of Selected Topics in Quantum Electronics, 23(2), 72-80.
32. Wang, X., Wu, X., Zhu, J., Pang, Z., Yang, H., & Qi, Y. (2019). Theoretical investigation of a highly sensitive refractive-index sensor based on TM0 waveguide mode resonance excited in an asymmetric metal-cladding dielectric waveguide structure. Sensors, 19(5), 1187.
33. Gierak, J., Madouri, A., Biance, A. L., Bourhis, E., Patriarche, G., Ulysse, C., & Jede, R. (2007). Sub-5 nm FIB direct patterning of nanodevices. Microelectronic engineering, 84(5-8), 779-783.
34. Wu, W., Yang, J., Zhang, J., Huang, J., Chen, D., & Wang, H. (2016). Ultra-high resolution filter and optical field modulator based on a surface plasmon polariton. Optics Letters, 41(10), 2310-2313.